

# Single-Scattering Optical Tomography: Simultaneous Reconstruction of Scattering and Absorption

Lucia Florescu<sup>1</sup>, John C. Schotland<sup>1</sup>, and Vadim A. Markel<sup>2</sup>

<sup>1</sup>*Department of Bioengineering, University of Pennsylvania, Philadelphia, PA 19104,*

<sup>2</sup>*Department of Radiology, University of Pennsylvania, Philadelphia, PA 19104*

(Dated: August 11, 2018)

## Abstract

We demonstrate that simultaneous reconstruction of scattering and absorption of a mesoscopic system using angularly-resolved measurements of scattered light intensity is possible. Image reconstruction is realized based on the algebraic inversion of a generalized Radon transform relating the scattering and absorption coefficients of the medium to the measured light intensity and derived using the single-scattering approximation to the radiative transport equation.

## I. INTRODUCTION

There is considerable interest in the development of techniques for three-dimensional optical imaging of biological systems. In this context, of particular importance is the imaging of mesoscopic systems, where the photon transport mean free path is of the same order as the system size [1]. For such systems none of the available optical ballistic imaging modalities [2]-[6] or the diffuse optical tomography [7] can be used. On the mesoscopic length scale, applications to biological systems include imaging of engineered tissues, semitransparent organisms, or superficial tissues. This article is the second in a series devoted to the problem of optical imaging in the mesoscopic scattering regime. In Ref. [8], we have proposed a novel imaging technique that uses angularly-selective measurements of scattered light intensity to reconstruct the attenuation coefficient of an inhomogeneous medium, assuming that the single-light scattering is dominant. The advantages of this Single-Scattering Optical Tomography (SSOT) technique include the linearity, well-posedness, and two-dimensional character of the associated inverse problem, as well as the possibility to perform image reconstruction based on single-projection measurements. Here we generalize the SSOT technique to simultaneously reconstruct the internal scattering and absorption properties of the medium.

We begin by presenting a brief review of the SSOT formalism introduced in Ref. [8]. We assume that the light transport in an inhomogeneous medium is described by the time-independent radiative transport equation (RTE) for the specific intensity  $I(\mathbf{r}, \hat{\mathbf{s}})$  of light at the position  $\mathbf{r}$  and flowing in the direction  $\hat{\mathbf{s}}$ ,

$$[\hat{\mathbf{s}} \cdot \nabla + \mu_a(\mathbf{r}) + \mu_s(\mathbf{r})] I(\mathbf{r}, \hat{\mathbf{s}}) = \mu_s(\mathbf{r}) \int A(\hat{\mathbf{s}}, \hat{\mathbf{s}}') I(\mathbf{r}, \hat{\mathbf{s}}') d^2 \hat{\mathbf{s}}' , \quad \mathbf{r} \in V . \quad (1)$$

Here  $\mu_a(\mathbf{r})$  and  $\mu_s(\mathbf{r})$  are the absorption and scattering coefficients, and  $A(\hat{\mathbf{s}}, \hat{\mathbf{s}}')$  is the scattering kernels normalized such that  $\int A(\hat{\mathbf{s}}, \hat{\mathbf{s}}') d^2 \hat{\mathbf{s}}' = 1$  for all  $\hat{\mathbf{s}}$ . The RTE (1) is equivalent to the integral equation

$$I(\mathbf{r}, \hat{\mathbf{s}}) = I_b(\mathbf{r}, \hat{\mathbf{s}}) + \int G_b(\mathbf{r}, \hat{\mathbf{s}}; \mathbf{r}', \hat{\mathbf{s}}') \mu_s(\mathbf{r}') A(\hat{\mathbf{s}}', \hat{\mathbf{s}}'') I(\mathbf{r}', \hat{\mathbf{s}}'') d^3 r' d^2 \hat{\mathbf{s}}' d^2 \hat{\mathbf{s}}'' , \quad (2)$$

where  $I_b(\mathbf{r}, \hat{\mathbf{s}})$  is the ballistic component of the specific intensity, and the ballistic Green's function  $G_b(\mathbf{r}, \hat{\mathbf{s}}; \mathbf{r}', \hat{\mathbf{s}}')$  is expressed as

$$G_b(\mathbf{r}, \hat{\mathbf{s}}; \mathbf{r}', \hat{\mathbf{s}}') = g(\mathbf{r}, \mathbf{r}') \delta \left( \hat{\mathbf{s}}' - \frac{\mathbf{r} - \mathbf{r}'}{|\mathbf{r} - \mathbf{r}'|} \right) \delta(\hat{\mathbf{s}} - \hat{\mathbf{s}}') , \quad (3)$$

with

$$g(\mathbf{r}, \mathbf{r}') = \frac{1}{|\mathbf{r} - \mathbf{r}'|^2} \exp \left[ - \int_0^{|\mathbf{r} - \mathbf{r}'|} \mu_t \left( \mathbf{r}' + \ell \frac{\mathbf{r} - \mathbf{r}'}{|\mathbf{r} - \mathbf{r}'|} \right) d\ell \right] \quad (4)$$

the angularly-averaged ballistic Green's function. Here  $\mu_t(\mathbf{r}) = \mu_a(\mathbf{r}) + \mu_s(\mathbf{r})$  is the extinction (attenuation) coefficient.

The light transport in a mesoscopic system is described by the first-order scattering approximation to the RTE. This corresponds to the assumption that light propagating in the inhomogeneous medium is just single scattered, and consists in replacing  $I(\mathbf{r}, \hat{\mathbf{s}})$  by  $I_b(\mathbf{r}, \hat{\mathbf{s}})$  in the right-hand side of Eq. (2). Consider that the medium is illuminated by a light beam of intensity  $I_0$  entering the slab at the point  $\mathbf{r}_1$  and in the direction  $\hat{\mathbf{s}}_1$ , and that an angularly-selective detector registers the ray exiting the slab through the opposite surface at the point  $\mathbf{r}_2$  and in the direction  $\hat{\mathbf{s}}_2$  (as shown in Fig. 1). The intensity measured in a such experiment is denoted by  $I_s(\mathbf{r}_2, \hat{\mathbf{s}}_2; \mathbf{r}_1, \hat{\mathbf{s}}_1)$ . Within the single-scattering approximation, a relationship between the scattering and absorption coefficients of the medium and the measured light intensity is derived in the form

$$\int_{\text{BR}(\mathbf{r}_2, \hat{\mathbf{s}}_2; \mathbf{r}_1, \hat{\mathbf{s}}_1)} \mu_t[\mathbf{r}(\ell)] d\ell - \ln \left[ \frac{\mu_s(\mathbf{R}_{21})}{\bar{\mu}_s} \right] = \phi(\mathbf{r}_2, \hat{\mathbf{s}}_2; \mathbf{r}_1, \hat{\mathbf{s}}_1) . \quad (5)$$

Here the integral  $\int_{\text{SSR}} \mu_t(\mathbf{r}(\ell)) d\ell$  of the attenuation function is evaluated along the *broken ray* (BR) (shown in Fig. 1), corresponding to single-scattered photons and uniquely defined by the source and detector positions and orientations,  $\ell$  is the linear coordinate on this ray,  $\mathbf{R}_{21}$  is the ray turning point, and  $\bar{\mu}_s$  is the average (background) value of the scattering coefficient. The data function  $\phi(\mathbf{r}_2, \hat{\mathbf{s}}_2; \mathbf{r}_1, \hat{\mathbf{s}}_1)$  is defined as

$$\phi(\mathbf{r}_2, \hat{\mathbf{s}}_2; \mathbf{r}_1, \hat{\mathbf{s}}_1) = - \ln \left[ \frac{r_{21} \sin \theta_1 \sin \theta_2 \int I_s(\mathbf{r}_2, \hat{\mathbf{s}}_2; \mathbf{r}_1, \hat{\mathbf{s}}_1) d\varphi_{\hat{\mathbf{s}}_2}}{I_0 \bar{\mu}_s A(\hat{\mathbf{s}}_2, \hat{\mathbf{s}}_1)} \right] , \quad (6)$$

where  $r_{21} = |\mathbf{r}_2 - \mathbf{r}_1|$ , the angles  $\theta_1$  and  $\theta_2$  are defined by  $\cos \theta_{1,2} = \hat{\mathbf{r}}_{21} \cdot \hat{\mathbf{s}}_{1,2}$ ,  $\varphi_{\hat{\mathbf{s}}_2}$  is the polar angle of  $\hat{\mathbf{s}}_2$ , and the scattering kernel  $A(\hat{\mathbf{s}}, \hat{\mathbf{s}}')$  is assumed position-independent and known.

Eq. (5) is applied to optical imaging in the following manner. The selection of incidence and detection points and incidence and detection directions defines a slice in which image reconstruction is performed. In Fig. 1, this slice coincides with the  $YZ$ -plane of the laboratory frame. Assuming that the  $x$ -coordinate is fixed, the absorption and scattering coefficients can be regarded as two-dimensional functions of variables  $(y, z)$ . On the other hand, the data are four-dimensional, depending, in general, on two spatial and two angular variables,

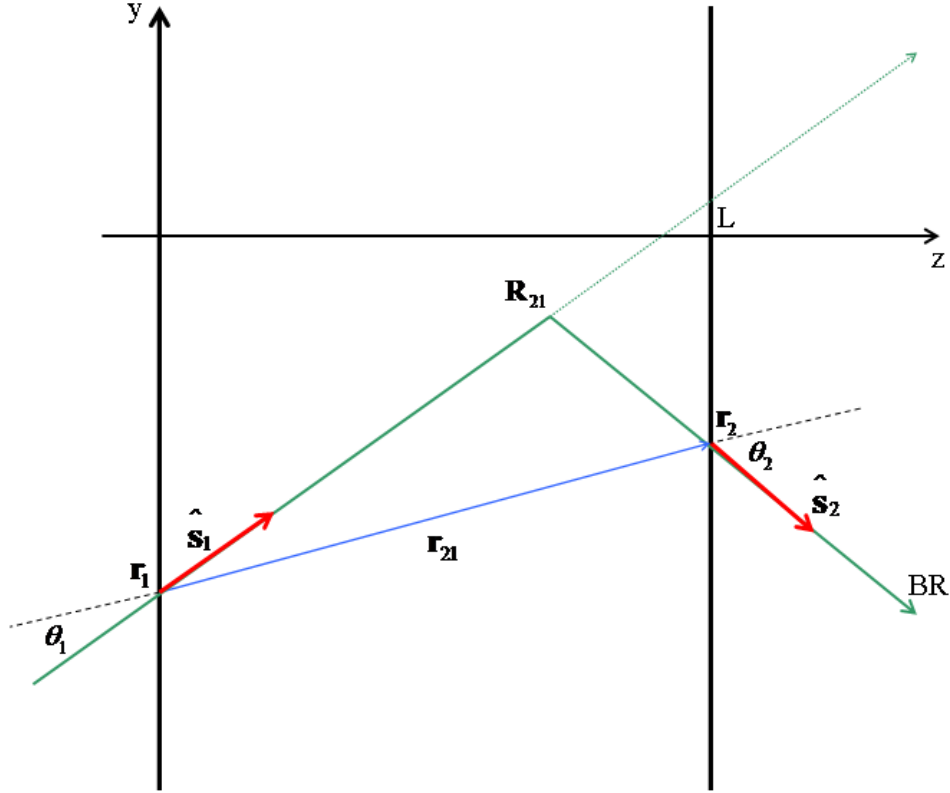


FIG. 1: (Color online) Geometrical illustration of the quantities used in Eq. (6) and elsewhere. “BR” denotes broken, single-scattered ray.

corresponding to the source and detection  $y$ -coordinate, and source and detection direction, respectively. This enables the simultaneous reconstruction of scattering and absorption. By utilizing multiple incident beams and detecting light exiting the medium at different points, and by varying the incident and exit angles, it is possible to collect enough data to reconstruct the absorption and scattering coefficients in a given slice. Three-dimensional reconstruction is then performed slice-by-slice.

In SSOT, simultaneous reconstruction of scattering and absorption can be in fact realized without scanning all parameter space. It is enough to keep the incidence direction (defined by the incidence angle  $\beta_1$ ) fixed, to scan the incidence point  $y_1$ , and for each such source realization to scan the detection point  $y_2$ , for each detection position considering just one detection direction, corresponding to the detection angle  $\beta_2 > \beta_1$ , if  $y_2 > y_1 + L \tan \beta_1$ , or to the angle  $-\beta_2$ , if  $y_2 < y_1 + L \tan \beta_1$ , where  $\beta_2$  is fixed and  $L$  is the slab thickness. The incidence and detection angles are the angles between the  $z$ -axis of the laboratory frame

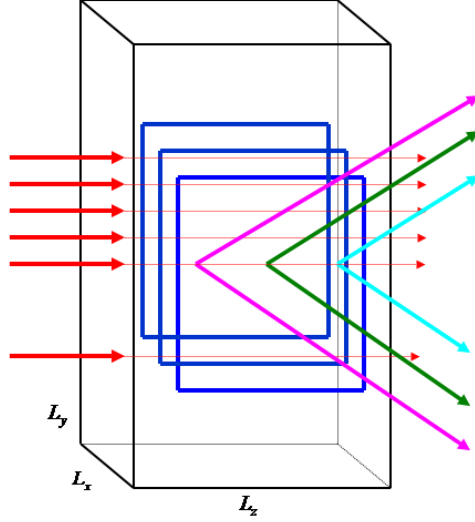


FIG. 2: (Color online) Schematic illustration of the proposed experiment geometry for simultaneous reconstruction of scattering and absorption. Reconstruction is performed in slices distributed along the  $x$  direction. The blue rectangles represent the areas in which reconstruction can be performed.

and the unit vectors  $\hat{\mathbf{s}}_1$  and  $\hat{\mathbf{s}}_2$ , respectively. This principle is schematically illustrated in Fig. 2 for a rectangular sample illuminated by a normally incident beam. In the presence of scattering, both ballistic and scattered rays are present. To avoid the detection of the ballistic component of the transmitted light, the angularly-selective source and detectors are not aligned with each other.

For a light beam entering the sample at position  $(y_1, z_1)$  and at the incident angle  $\beta_1$ , consider pairs of detections defined by the detection position and detection angle  $(y_2, z_2)$  and  $\beta_2 > \beta_1$ , and  $(y'_2, z_2)$  and  $-\beta_2$ , respectively, where  $y_2 > y_1 + L \tan \beta_1$ ,  $y'_2 = y_2 - 2(z_2 - z_0) \tan \beta_2$ , and  $z_0 = (z_2 \tan \beta_2 - z_1 \tan \beta_1) / (\tan \beta_2 - \tan \beta_1) - (y_2 - y_1) / (\tan \beta_2 - \tan \beta_1)$ . This two measurements corresponds to rays single-scattered at the same position  $\mathbf{R}_{21} = (y_0, z_0)$  within the sample, where  $y_0 = (z_2 - z_0) \tan \beta_2$ . Such rays are shown by the same color in Fig. 2. Writing Eq. (5) for the two situations and then subtracting the corresponding equations, one obtains the following equation:

$$\int_{\text{BR}(y_2, \beta_2; y_1, \beta_1)} \mu_t[y(\ell), z(\ell)] d\ell - \int_{\text{BR}(y'_2, -\beta_2; y_1, \beta_1)} \mu_t[y(\ell), z(\ell)] d\ell = \phi(y_2, \beta_2; y_1, \beta_1) - \phi(y'_2, -\beta_2; y_1, \beta_1). \quad (7)$$

Here the integrals of the total attenuation coefficient are along the two single-scattered

rays described above, and  $\phi(y_2, \beta_2; y_1, \beta_1)$  and  $\phi(y_2', -\beta_2; y_1, \beta_1)$  are the data functions corresponding to the two detections. Eq. (7) can be solved with respect to  $\mu_t(y, z)$ . Then Eq. (5) written for one of the detections can be solved for  $\ln[\mu_s(y, z)/\langle\mu_s\rangle]$ . From these two solutions,  $\mu_a(y, z)$  and  $\mu_s(y, z)$  can be determined.

## II. IMAGE RECONSTRUCTION

In what follows, we illustrate simultaneous reconstruction of scattering and absorption in SSOT based on the algebraic inversion of Eq. (5). We note that a more sophisticated image reconstruction algorithm based on an inverse formula is also possible and will be presented elsewhere.

The forward data is obtained by solving Eq. (2) numerically, along the lines presented in detail in Ref. [8], generalized here for the case of a homogeneously scattering medium. For isotropic scattering ( $A(\hat{\mathbf{s}}, \hat{\mathbf{s}}) = 1/4\pi$ ), Eq. (2) takes the form

$$I(\mathbf{r}, \hat{\mathbf{s}}) = I_b(\mathbf{r}, \hat{\mathbf{s}}) + \int G_b(\mathbf{r}, \hat{\mathbf{s}}; \mathbf{r}', \hat{\mathbf{s}}') \frac{\mu_s(\mathbf{r}')}{4\pi} u(\mathbf{r}') d^3 r' d^2 \hat{\mathbf{s}}'. \quad (8)$$

Here  $u(\mathbf{r}) \equiv \int I(\mathbf{r}, \hat{\mathbf{s}}) d^2 \hat{\mathbf{s}}$  is the density of electromagnetic energy satisfying the following integral equation

$$u(\mathbf{r}) = u_b(\mathbf{r}) + \int g_b(\mathbf{r}, \mathbf{r}') \frac{\mu_s(\mathbf{r}')}{4\pi} u(\mathbf{r}') d^3 r', \quad (9)$$

where  $u_b(\mathbf{r}) \equiv \int I_b(\mathbf{r}, \hat{\mathbf{s}}) d^2 \hat{\mathbf{s}}$  is the “ballistic density”. The scattered component of the intensity,  $I_s = I - I_b$ , is computed by solving first Eq. (9) and then substituting the numerical solution  $u(\mathbf{r})$  into (8). We emphasize that this numerical approach is non-perturbative and includes all scattering orders, similarly to the experimental situation when all scattered light is detected.

Equation (9) is discretized on a rectangular grid and solved by methods of linear algebra. The energy density  $u(\mathbf{r})$  and the scattering and absorption coefficients are assumed constant within each cubic cell. The corresponding values  $u_n = u(\mathbf{r}_n)$ , where  $\mathbf{r}_n$  is the center of the  $n$ -th cubic cell, obey the algebraic system of equations

$$(1 - R_{\text{eq}}\mu_s(\mathbf{r}_n)) u_n - \frac{h^3}{4\pi} \sum_{m \neq n} g_b(\mathbf{r}_n, \mathbf{r}_m) \mu_s(\mathbf{r}_m) u_m = u_b(\mathbf{r}_n). \quad (10)$$

Here  $h$  is the discretization step,  $u_b(\mathbf{r}_n) \equiv h^{-3} \int_{V_n} u_b(\mathbf{r}) d^3r$ , and  $R_{\text{eq}} = (3/4\pi)^{1/3}h$  is the radius of a sphere of equivalent volume to that of a cell, introduced to compute the diagonal matrix elements of the system (10) [8]. The system of equations (10) is solved by direct matrix inversion, and then the specific intensity is calculated according with the discretized version of (8),

$$I(\mathbf{r}_2, \hat{\mathbf{s}}_2) = \frac{h^3}{4\pi} \sum_{\mathbf{r}_2 - \mathbf{r}_n = \hat{\mathbf{s}}_2 |\mathbf{r}_2 - \mathbf{r}_n|} g_b(\mathbf{r}_2, \mathbf{r}_n) \mu_s(\mathbf{r}_n) u_n, \quad (11)$$

where the summation is performed only over such cells that are intersected by the ray exiting from the detection point  $\mathbf{r}_2$  in the direction  $\hat{\mathbf{s}}_2$ . The data function is calculated in terms of the average of the specific intensity over the cell,  $\bar{I}(\mathbf{r}_2, \hat{\mathbf{s}}_2) \equiv (1/h^3) \int d\mathbf{r}_2 I(\mathbf{r}_2, \hat{\mathbf{s}}_2)$ . To model noise in the measured data,  $\bar{I}(\mathbf{r}_2, \hat{\mathbf{s}}_2)$  was scaled and rounded off so that it was represented by 16-bit unsigned integers, similar to the measurement by digital ccd cameras. Then a statistically-independent positively-defined random variable was added to each measurement  $\bar{I}(\mathbf{r}_2, \hat{\mathbf{s}}_2)$ . The random variables were evenly distributed in the interval  $[0, nI_{\text{av}}]$ , where  $n$  is the noise level and  $I_{\text{av}}$  is the average measured intensity (a 16-bit integer). The data function is calculated using the discretized version of Eq. (6),

$$\phi(y_2, \beta_2; y_1, \beta_1) = -\ln \left[ \frac{4\pi}{h^3} \frac{\bar{I}(\mathbf{r}_2, \hat{\mathbf{s}}_2)}{I_0 \bar{\mu}_s} \right]. \quad (12)$$

Image reconstruction for the attenuation coefficient is obtained using Eqs. (5) and (7), which are discretized on the same grid as the one used for obtaining the forward solution, except that in this case planar slices with fixed  $x$ -coordinates are used. The discrete version of (7) is

$$\sum_n \mathcal{L}_{\nu n} \mu_{tn} = \phi_\nu, \quad (13)$$

where the index  $\nu = (y_1, \beta_1; y_2, \beta_2)$  corresponds to a given realization of the source and detection pair, and  $\mathcal{L}_{\nu n} = \mathcal{L}_{\nu n}^{(1)} - \mathcal{L}_{\nu n}^{(2)}$ , with the matrix element  $\mathcal{L}_{\nu n}^{(i)}$  given by the length of the intersection of the detected ray  $i$  with the  $n$ -th cubic cell.  $\phi_\nu = \phi_\nu^{(1)} - \phi_\nu^{(2)}$ , with  $\phi_\nu^{(i)}$  the data function corresponding to the ray  $i$ . Eq. (16) is solved for  $\mu_{tn}$  by regularized SVD pseudoinverse [9], namely

$$|\mu_t^+\rangle = (\mathcal{L}^* \mathcal{L})^{-1} \mathcal{L}^* |\phi\rangle, \quad (14)$$

where

$$(\mathcal{L}^* \mathcal{L})^{-1} = \sum_n \Theta(\sigma_n^2 - \epsilon) \frac{|f_n\rangle \langle f_n|}{\sigma_n^2}. \quad (15)$$

Here  $\Theta(x)$  is the step function,  $\epsilon$  is a small regularization parameter, and  $|f_n\rangle$  and  $\sigma_n$  are the singular functions and singular values, respectively, of the matrix  $\mathcal{L}$ , obtained by solving the symmetric eigenproblem  $\mathcal{L}^* \mathcal{L} |g_n\rangle = \sigma_n^2 |g_n\rangle$ . Further, the scattering coefficient is determined from Eq. (5), discretized as

$$\sum_n \mathcal{L}_{\nu n}^{(1)} \mu_{tn} - \ln \left[ \frac{\mu_s(\mathbf{R}_{21})}{\bar{\mu}_s} \right] = \phi_\nu^{(1)}(y_2, \beta_2; y_1, \beta_1). \quad (16)$$

Finally, the absorption coefficient is obtained as  $\mu_{an} = \mu_{tn} - \mu_{sn}$ .

### A. Numerical Results

We considered a rectangular isotropically scattering sample of dimensions  $L_x = 25h$ ,  $L_y = 122h$  and  $L_z = 40h$ . The background scattering coefficient is chosen such that the optical depth  $\bar{\mu}_s L_z$  is 1.6. This corresponds to the mesoscopic scattering regime in which the image reconstruction method of SSOT is applicable. The background absorption coefficient is set equal to  $\bar{\mu}_a = 0.1\bar{\mu}_s$ . The target is a set of inclusions concentrated in the layers  $x = 6h$ ,  $x = 13h$  and  $x = 20h$ .

Image reconstruction is performed in slices  $x = x_{\text{slice}} = \text{const}$  separated by the distance  $\Delta x = h$ . The reconstruction area inside each slice is  $44h \leq y \leq 77h$ ,  $4h \leq z \leq 37h$ , with the field of view  $34h \times 34h$ . For each slice, the sources are normally incident ( $\beta_1 = 0$ ) on the surface  $z = 0$  at the positions  $x = x_{\text{slice}}$ ,  $y = y_s = nh$ ,  $z = 0$ , with  $n$  integers. The detectors are placed on the opposite side of the sample at positions  $x = x_{\text{slice}}$ ,  $y = y_d = nh$ ,  $z = L_z$  and measure the specific intensity exiting the surface  $z = L_z$  at the angle of  $\beta_2 = \pi/4$ , for  $y_d > y_s$ , and  $-\pi/4$ , for  $y_d < y_s$ , with respect to the  $z$ -axis.

First, we considered the case of purely absorbing inhomogeneities, spatially modulated as shown in Fig. 4 in the column marked ‘‘Model’’. The scattering coefficient is constant throughout the sample and equal to the background value. The absorption coefficient for the inhomogeneities in the slice  $x = 6h$  is set to  $\mu_a = 2\bar{\mu}_a$  and  $\mu_a = 5\bar{\mu}_a$ , for the outer and inner square, respectively. In slices  $x = 13h$  and  $x = 20h$  there are more absorbing inhomogeneities, of absorbing coefficient  $\mu_a = 2\bar{\mu}_a, 4\bar{\mu}_a, 5\bar{\mu}_a$ , going from the outmost to the innermost square. Thus, the contrast of  $\mu_t$  (the ratio of  $\mu_t$  in the target to the background

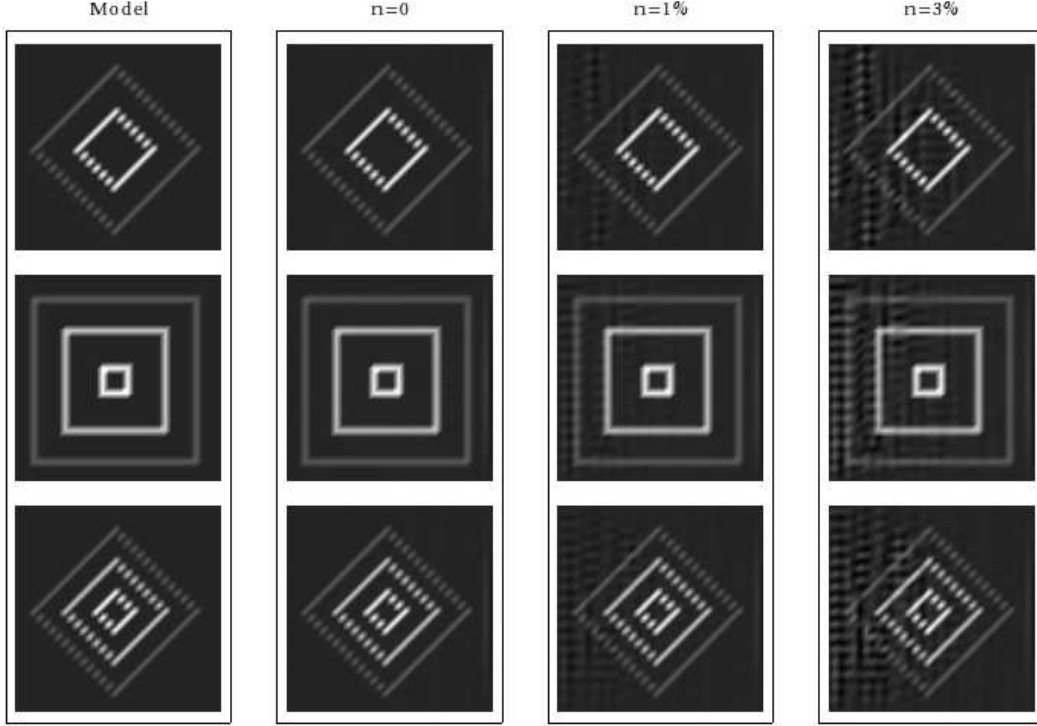


FIG. 3: (Color online) Image reconstruction for the total attenuation coefficient  $\mu_t$  for a homogeneously scattering sample with  $\bar{\mu}_s L_z = 1.6$  and  $\bar{\mu}_a = 0.1\bar{\mu}_s$ , and for various noise levels  $n$ . The rows show the slices  $x = 6h$ ,  $13h$  and  $20h$ , where the absorbing inhomogeneities are placed. The contrast in  $\mu_t$  varies from 1.09 to 1.36.

value) varies from 1.09 for the outmost squares in each slice to 1.36 for the innermost square. The results of image reconstruction for the total attenuation coefficient  $\mu_t$  and absorption coefficient  $\mu_a$  for various noise levels  $n$  are presented in Figs. 3 and 4. Only the slices containing inhomogeneities are shown. The other slices present no features, which means that no cross-talk exists between various slices, as it was also demonstrated previously [8]. It can be seen that the spatial resolution of images depends on the noise level and can be as good as one discretization step,  $h$ . Note that image reconstruction is in very good quantitative agreement with the model (all panels in each figure are plotted using the same color scale) and stable in the presence of noise. Note also that the two-angle measurement scheme considered here enables better image reconstruction of the attenuation coefficient than the single-angle scheme considered previously [8].

Consider now the case when scattering inhomogeneities are also present in the system and

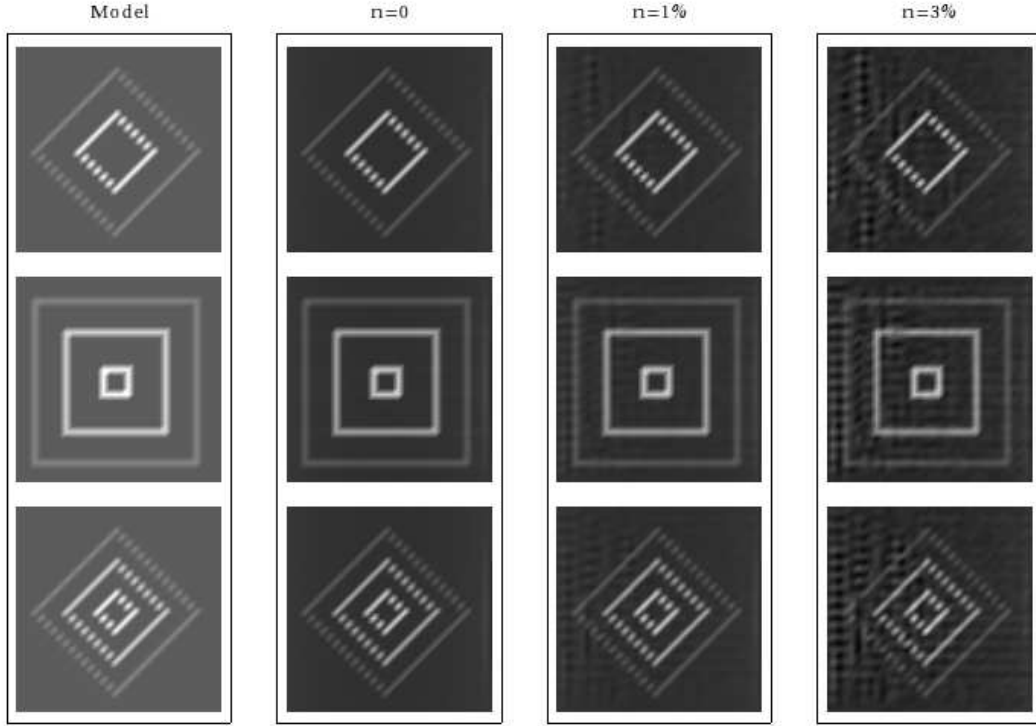


FIG. 4: (Color online) Image reconstruction for the absorption coefficient  $\mu_a$  for a homogeneously scattering sample with  $\bar{\mu}_s L_z = 1.6$  and  $\bar{\mu}_a = 0.1\bar{\mu}_s$ , and for various noise levels  $n$ . The rows show the slices  $x = 6h$ ,  $13h$  and  $20h$ , where the absorbing inhomogeneities are placed. The contrast in  $\mu_a$  varies from 2 to 5.

are spatially modulated as shown in Fig. 6 in the column marked “Model”, the absorption being modulated as described above. The scattering coefficients for the inhomogeneities in the slice  $x = 6h$  is set to  $\mu_s = 1.33\bar{\mu}_s$  and  $\mu_s = 1.66\bar{\mu}_s$ , for the outer and inner square, respectively, and in this slice the absorbing and scattering inhomogeneities overlap with each other. In the slice  $x = 13h$ , there are more scattering inhomogeneities as compared to the slice  $x = 6h$ , the scattering coefficient is  $\mu_s = 1.33\bar{\mu}_s, 1.66\bar{\mu}_s, 1.66\bar{\mu}_s$ , going from the outermost to the innermost inhomogeneity, and the absorbing and scattering inhomogeneities do not overlap. In the slice  $x = 20h$ , the absorbing and scattering inhomogeneities overlap, the scattering coefficient is modulated the same as in slice  $x = 13h$  except that its value for the innermost inhomogeneity is larger,  $\mu_s = 2\bar{\mu}_s$ . For this sample, the contrast of  $\mu_t$  varied from 1.09 for the utmost squares in slice  $x = 13$  to 2.27 for the innermost square in slice  $x = 20$ . Image reconstruction in this case is presented in Figs. 5-7. Very good image

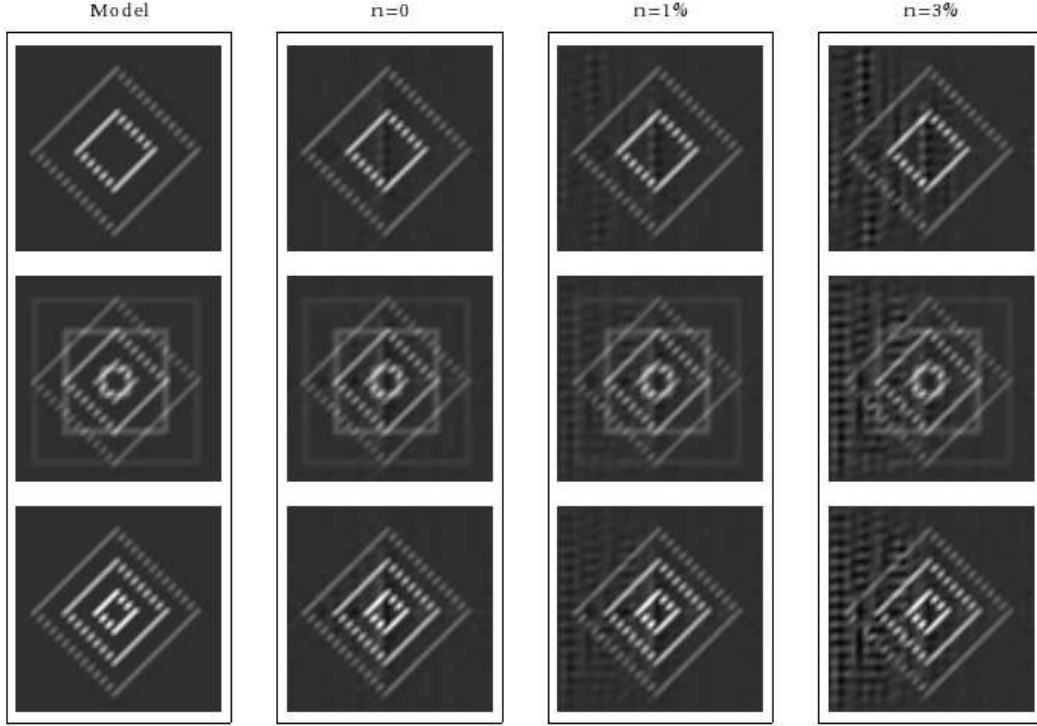


FIG. 5: (Color online) Image reconstruction for the total attenuation coefficient  $\mu_t$  for an inhomogeneously scattering and absorbing sample and for various noise levels  $n$ . The rows show the slices  $x = 6h$ ,  $13h$  and  $20h$ , where the inhomogeneities are placed. The background scattering and absorption coefficients are set such that  $\bar{\mu}_s L_z = 1.6$  and  $\bar{\mu}_a = 0.1\bar{\mu}_s$ , the contrast in  $\mu_s$  varies from 1.33 to 2, the contrast in  $\mu_a$  varies from 2 to 5, and the contrast in  $\mu_t$  varies from 1.09 to 2.27.

quality is obtained for both the total attenuation coefficient and scattering coefficient, image reconstruction for scattering being less influenced by the noise in the data function. On the other hand, image quality for absorption is notably lower. However, most of the relevant features are legible.

Further, consider stronger scattering inhomogeneities and perform image reconstruction for a sample in which the scattering coefficient of the inhomogeneities is spatially modulated the same as in the previous case, but it is increased by a factor of 1.5, the absorbing inhomogeneities having the same characteristics. Thus, in this case, the contrast in the scattering coefficient varies from 2 for the outermost inhomogeneity in each slice to 3 for the innermost inhomogeneity in slice  $x = 20$ . The contrast in  $\mu_t$  varies from 1.09 to 3.18. The results are presented in Figs. 8-10. Very good image reconstruction is obtained for both the

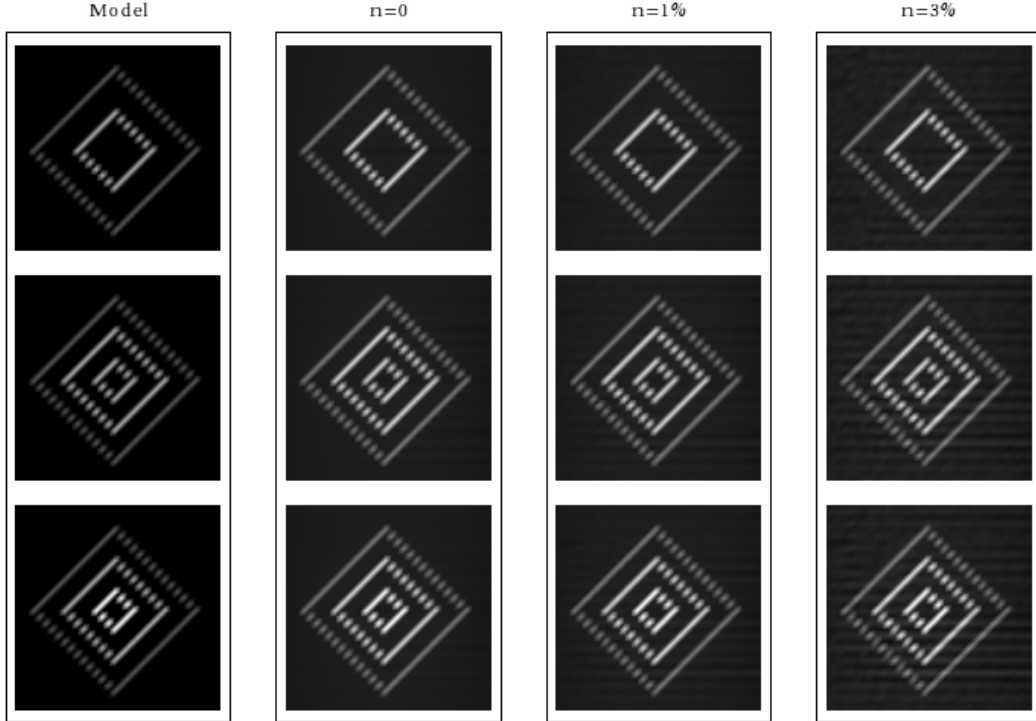


FIG. 6: (Color online) Image reconstruction for the scattering coefficient  $\mu_s$  for an inhomogeneously scattering and absorbing sample and for various noise levels  $n$ . The rows show the slices  $x = 6h$ ,  $13h$  and  $20h$ , where the inhomogeneities are placed. The background scattering and absorption coefficients are set such that  $\bar{\mu}_s L_z = 1.6$  and  $\bar{\mu}_a = 0.1\bar{\mu}_s$ , the contrast in  $\mu_s$  varies from 1.33 to 2, and the contrast in  $\mu_a$  varies from 2 to 5.

total attenuation and scattering coefficients, but image reconstruction for absorption is very poor.

The reconstructed image quality is determined by two factors, the amount of scattering in the system and the noise in the data. In particular, for stronger scattering, the single-scattering approximation we employ may be inaccurate, leading to poor image reconstruction. In order to separate the influence of these factors on the image quality, we perform image reconstruction based on a data function corresponding only to single-scattered light, obtained using the so-called inverse crime. This consists of generating data using the same model that the inverse solver is based on. Specifically, instead of solving RTE numerically and using the solution to calculate the data function according to the definition (6), the data function is calculated from (7), derived within the single-scattering approximation of RTE,

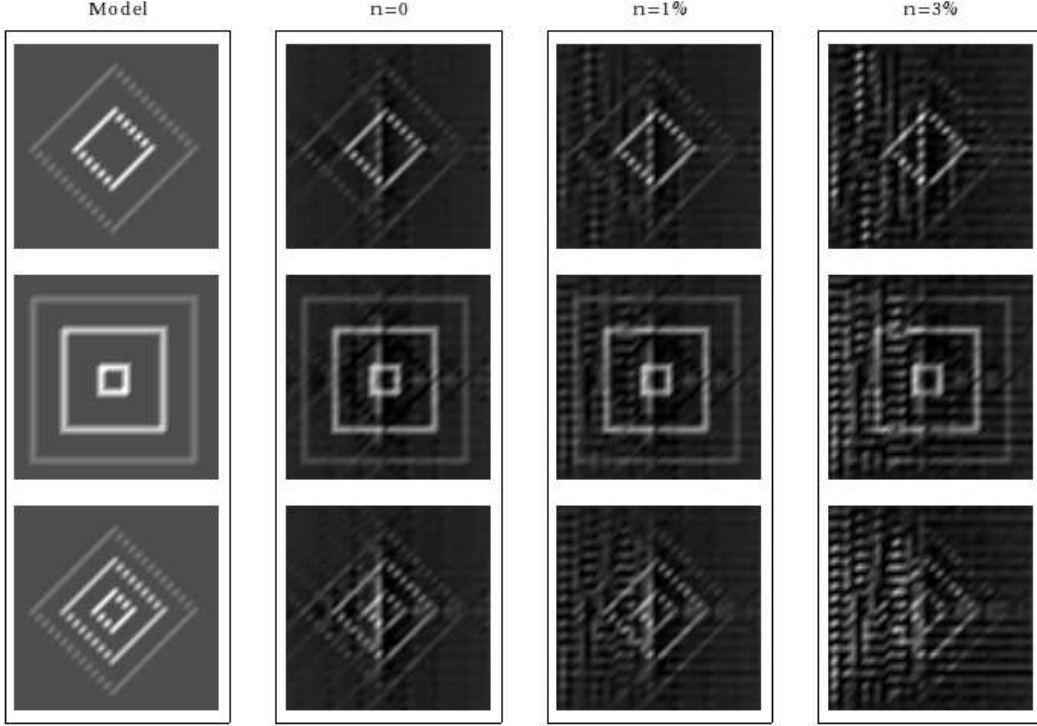


FIG. 7: (Color online) image reconstruction for the absorption coefficient  $\mu_a$  for an inhomogeneously scattering and absorbing sample and for various noise levels  $n$ . The rows show the slices  $x = 6h$ ,  $13h$  and  $20h$ , where the inhomogeneities are placed. The background scattering and absorption coefficients are set such that  $\bar{\mu}_s L_z = 1.6$  and  $\bar{\mu}_a = 0.1\bar{\mu}_s$ , the contrast in  $\mu_s$  varies from 1.33 to 2, and the contrast in  $\mu_a$  varies from 2 to 5.

by replacing the extinction and scattering coefficients by those of the model. In this case, the influence of the amount of scattering in the sample on the image quality is eliminated, the only influence coming from the noise in the data. Image reconstruction for the same sample that was analyzed in Figs. 8-10 is presented in Figs. 11-13. By comparing these two sets of results, one can see that the image quality for the attenuation and scattering coefficients is almost the same in both cases. Therefore, it can be concluded that the single-scattering approximation works very well for the scattering strength considered and that, in this scattering regime, the most influence on the image quality comes from the noise in the data. Moreover, Figs. 11-13 show that the reconstructed coefficients experience various levels of influence from the noise in the data. While the reconstructed attenuation and scattering coefficients are very little influenced by the noise, the absorption coefficient experiences a

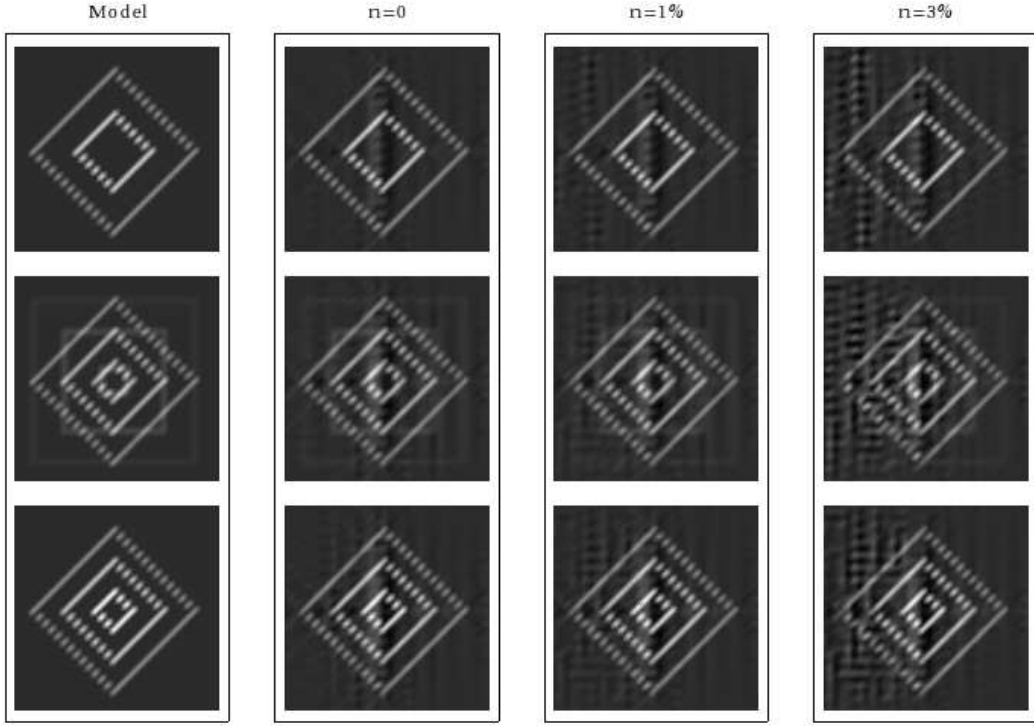


FIG. 8: (Color online) Image reconstruction for the total attenuation coefficient  $\mu_t$  for an inhomogeneously scattering and absorbing sample and for various noise levels  $n$ . The rows show the slices  $x = 6h$ ,  $13h$  and  $20h$ , where the inhomogeneities are placed. The background scattering and absorption coefficients are set such that  $\bar{\mu}_s L_z = 1.6$  and  $\bar{\mu}_a = 0.1\bar{\mu}_s$ , the contrast in  $\mu_s$  varies from 2 to 3, the contrast in  $\mu_a$  varies from 2 to 5, and the contrast in  $\mu_t$  varies from 1.09 to 3.18.

much stronger influence, imagine quality being very poor even for a noise level of 3% in the measured intensity.

To explain the various levels of influence of the noise in the data on the image quality, we perform a rough error propagation analysis. Assume that the scattered intensity  $I_s$  is determined with an error  $\delta I_s$ . From Eq. (14) and the definition (6) of the data function, it follows that the noise in the data results in a noise  $\delta\mu_{tn}$  in the total attenuation coefficient given by

$$\delta\mu_{tn} = \sqrt{2} \frac{\delta I_s}{I_s} \left( \sum_m \frac{|f_{mn}|^2}{\sigma_m^2} \Theta(\sigma_m^2 - \epsilon) \right)^{1/2}. \quad (17)$$

Here, we have assumed that the relative error in determining the scattered intensity is the same for the symmetric measurements used to reconstruct  $\mu_t$ , and the factor  $\sqrt{2}$  results from

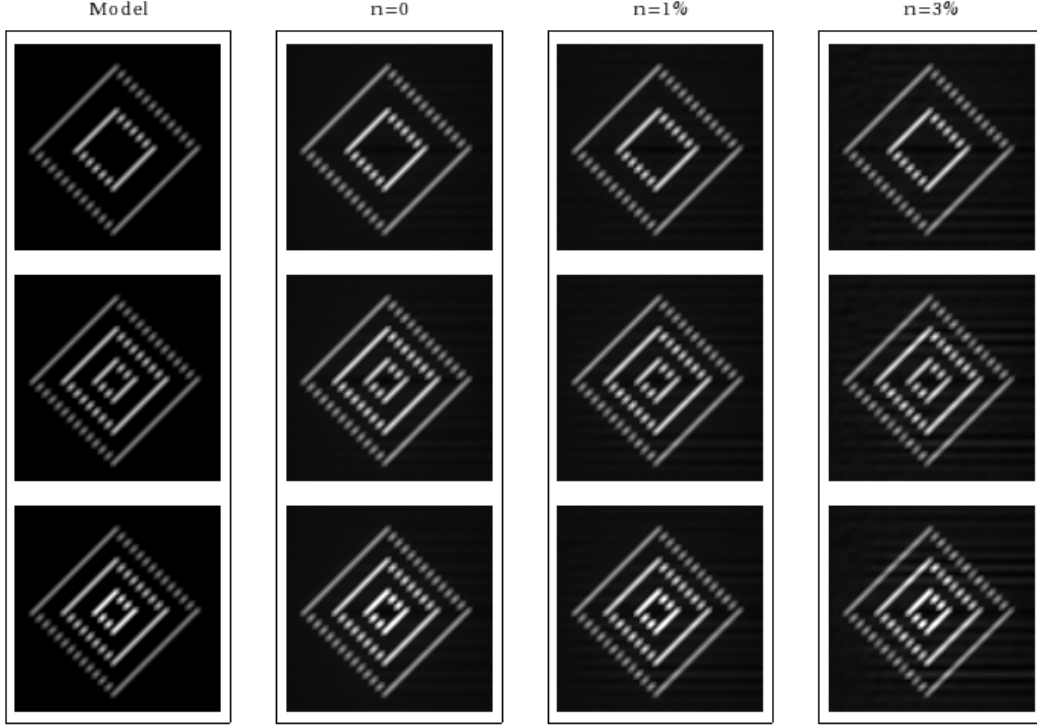


FIG. 9: (Color online) Image reconstruction for the scattering coefficient  $\mu_s$  for an inhomogeneously scattering and absorbing sample and for various noise levels  $n$ . The rows show the slices  $x = 6h$ ,  $13h$  and  $20h$ , where the inhomogeneities are placed. The background scattering and absorption coefficients are set such that  $\bar{\mu}_s L_z = 1.6$  and  $\bar{\mu}_a = 0.1\bar{\mu}_s$ , the contrast in  $\mu_s$  varies from 2 to 3, and the contrast in  $\mu_a$  varies from 2 to 5.

using the the difference in the data functions corresponding to these measurements. On the other hand, the noise  $\delta\mu_{sn}$  in the scattering coefficient  $\mu_{sn}$  is estimated from Eqs. (16) and (17) to be

$$\frac{\delta\mu_{sn}}{\mu_{sn}} = \frac{\delta I_s}{I_s} \left( 1 + 2 \sum_i (L_{\nu i}^{(1)})^2 \sum_m \frac{|g_{mi}|^2}{\sigma_m^2} \Theta(\sigma_m^2 - \epsilon) \right)^{1/2}. \quad (18)$$

Here  $n$  labels the cell where the detected rays corresponding to the source-detection realization  $\nu$  are single scattered. Finally, the absorption coefficient is determined as the difference between the total attenuation coefficient and the scattering coefficient with the error  $\delta\mu_{an}$  that verifies

$$\frac{\delta\mu_{an}}{\mu_{an}} = \frac{\mu_{sn}}{\mu_{an}} \left[ \left( \frac{\delta\mu_{sn}}{\mu_{sn}} \right)^2 + \left( \frac{\mu_{tn}}{\mu_{sn}} \right)^2 \left( \frac{\delta\mu_{tn}}{\mu_{tn}} \right)^2 \right]^{1/2} > \frac{\mu_{sn}}{\mu_{an}} \frac{\delta I_s}{I_s}. \quad (19)$$

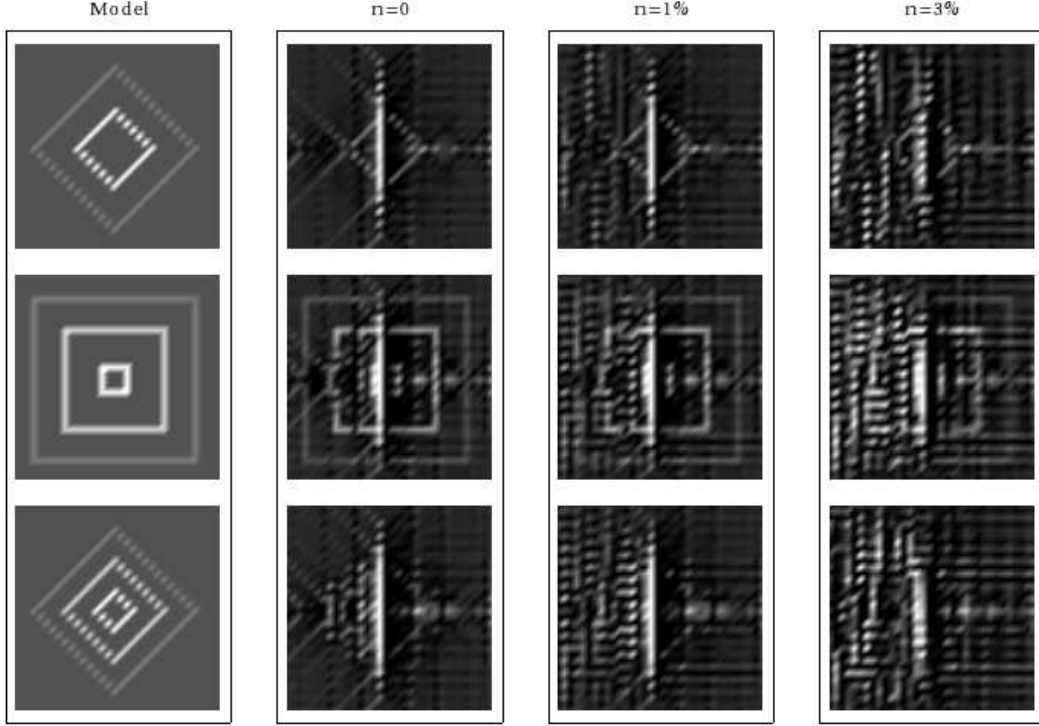


FIG. 10: (Color online) Image reconstruction for the absorption coefficient  $\mu_a$  for an inhomogeneously scattering and absorbing sample and for various noise levels  $n$ . The rows show the slices  $x = 6h$ ,  $13h$  and  $20h$ , where the inhomogeneities are placed. The background scattering and absorption coefficients are set such that  $\bar{\mu}_s L_z = 1.6$  and  $\bar{\mu}_a = 0.1\bar{\mu}_s$ , the contrast in  $\mu_s$  varies from 2 to 3, and the contrast in  $\mu_a$  varies from 2 to 5.

This expresses the fact that for samples where the absorption is stronger than the scattering, very large noise to signal levels in the reconstructed absorption coefficient result, even for low noise levels in the data. This result completely explains the image reconstruction for the absorption coefficient presented above. The difference between Figs. 7 and 10 is that the maximum value of the ratio  $\mu_s/\mu_a$  is increased from 4 (for Fig. 7) to 6 (for Fig. 10), leading to pronounced noise in the reconstructed image. Also, although stronger scattering inhomogeneities are present in slice  $x = 13$  (second row) in Fig. 10, better image quality is obtained compared with the slice  $x = 6$  (first row), since in this case the absorbing and scattering inhomogeneities do not overlap and  $\mu_s/\mu_a$  is smaller. The physical interpretation of this result is that the SSOT data function carries more signature of the scattering coefficient than of the absorption. In other words, in SSOT, the scattering coefficient is privileged

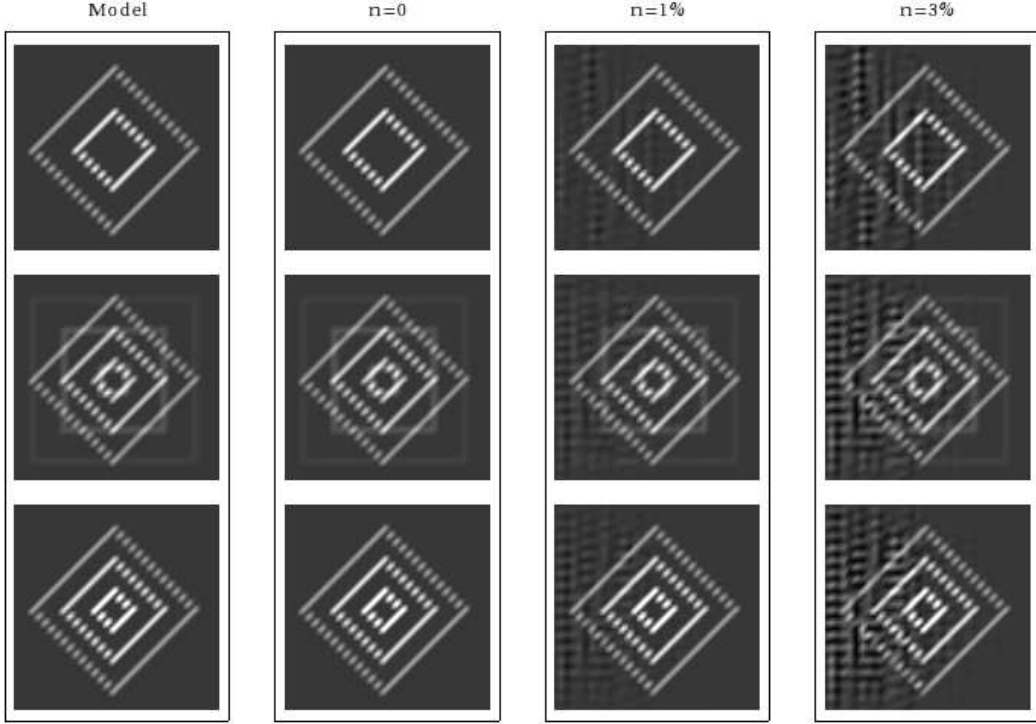


FIG. 11: (Color online) Image reconstruction for the total attenuation coefficient  $\mu_t$  for various noise levels  $n$ , for a data function corresponding only to single-scattered light and calculated according with (7) (inverse crime). All the sample parameters are as for Fig. 8.

as compared with the absorption coefficient. This fact originates from the RTE equation we employ, where the scattering coefficient has a stronger contribution than the absorption coefficient, and is also expressed by Eqs. (6) and (7), showing that the scattered intensity decays exponentially with the absorption coefficient, but has a stronger dependence on the scattering coefficient. In this case, besides the attenuation of the specific intensity as a result of absorption and scattering of photons from a given mode into other modes, there is also amplification of a given mode due to scattering of photons from other modes into that mode. We note that this dependence of the measured intensity of the scattering and absorption coefficients of the sample is different from the case of diffuse optical tomography. In the case of diffusive light propagation, the scattering of photons into and out various directional modes does not affect the light intensity, the diffusion equation has similar contributions from the scattering and absorption coefficients, and the light intensity emerging from the sample decays exponentially with both  $\mu_s$  and  $\mu_a$ .

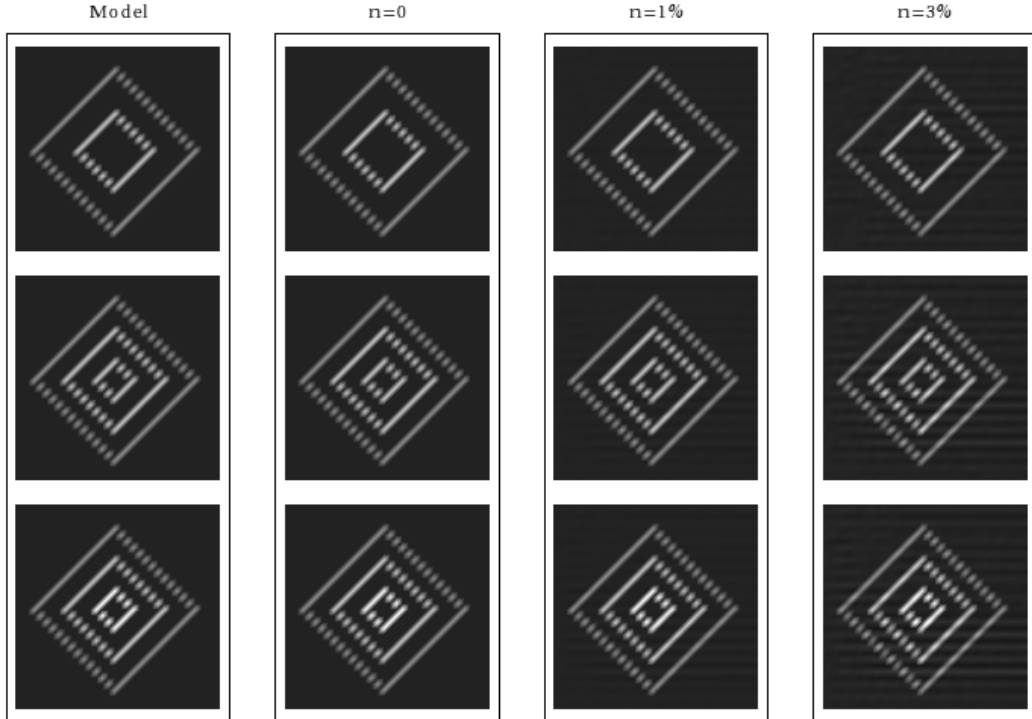


FIG. 12: (Color online) Image reconstruction for the scattering coefficient  $\mu_s$  for various noise levels  $n$ , for a data function corresponding only to single-scattered light and calculated according with (7) (inverse crime). All the sample parameters are as for Fig. 9.

To verify the conclusion presented above, we perform image reconstruction for a stronger absorbing sample. Figs. 14-16 present image reconstruction for a sample where the absorption and scattering are spatially modulated as for Figs. 8-10, but the absorption coefficient is increased by a factor of 10, such that it becomes comparable to the scattering coefficient. Indeed, the image reconstruction for the absorption coefficient presented in Fig. 16 is markedly better than in Fig. 10 and comparable to that for the scattering coefficient presented in Fig. 15.

Finally, we perform image reconstruction for a stronger scattering sample, characterized by an optical depth of the background of  $\bar{\mu}_s L_z = 3.2$  and an additional contrast in the scattering coefficient of up to 3. This is a borderline case when scattering is sufficiently strong so that the single-scattering approximation of SSOT may be expected to be inaccurate. The results for image reconstruction obtained for the case when the scattering and absorption have comparable strengths are presented in Figs. 17-19. We obtain that even in this

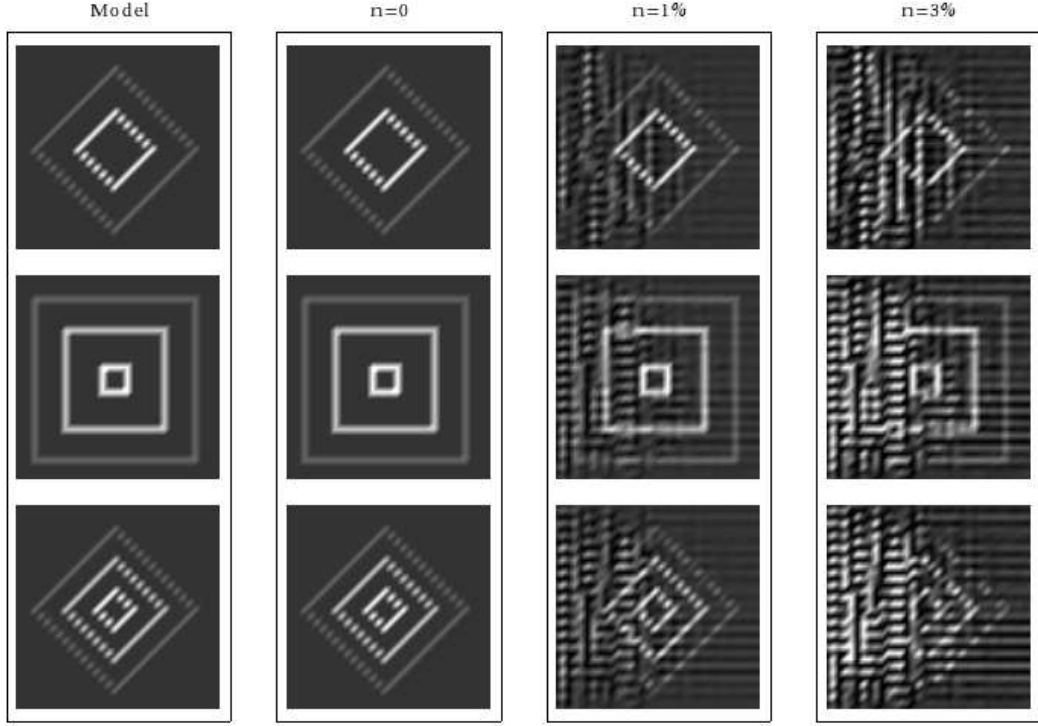


FIG. 13: (Color online) Image reconstruction for the absorption coefficient  $\mu_a$  for various noise levels  $n$ , for a data function corresponding only to single-scattered light and calculated according with (7) (inverse crime). All the sample parameters are as for Fig. 10.

scattering regime the most relevant features in the reconstructed scattering and absorption coefficients remain legible.

### III. CONCLUSIONS

We have demonstrated that the SSOT technique enables simultaneous reconstruction of scattering and absorption properties of mesoscopic systems. In particular, we have shown that while accurate, qualitative image reconstruction of scattering is always possible, good image reconstruction for absorption can be realized under the condition that scattering and absorption have comparable strengths. These conclusions have been reached under the assumption that the light propagating in the mesoscopic systems is just single scattered, but without making any assumption of measuring just single-scattered light. We have argued that better image quality for scattering as compared to absorption is possible since the SSOT

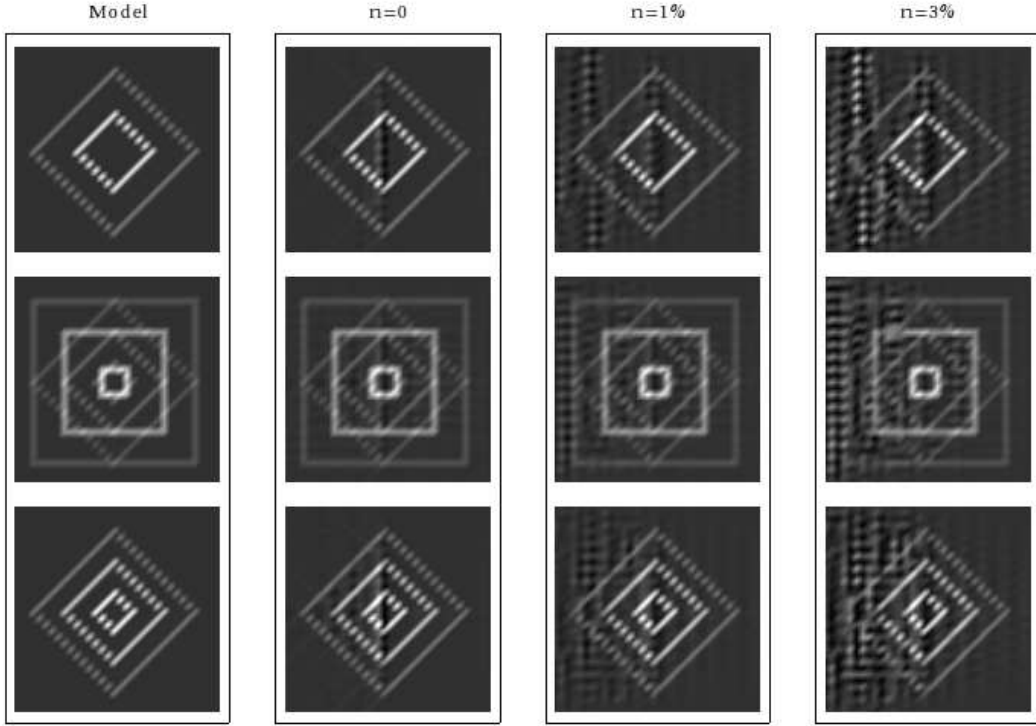


FIG. 14: (Color online) Image reconstruction for the total attenuation coefficient  $\mu_t$  for an inhomogeneously scattering and absorbing sample and for various noise levels  $n$ . The rows show the slices  $x = 6h$ ,  $13h$  and  $20h$ , where the inhomogeneities are placed. The background scattering and absorption coefficients are set such that  $\bar{\mu}_s L_z = 1.6$  and  $\bar{\mu}_a = \bar{\mu}_s$ , the contrast in  $\mu_s$  varies from 2 to 3, the contrast in  $\mu_a$  varies from 2 to 5, and the contrast in  $\mu_t$  varies from 2 to 4.

data function carries a stronger signature of scattering than of absorption.

Simultaneous reconstruction of scattering and absorption of mesoscopic systems can be experimentally implemented by appropriately choosing the wavelength of the illuminating beam, such that the effects of absorption and scattering have comparable strengths [10]. Alternatively, the absorption characteristics of the sample can be recovered through fluorescent SSOT, which will be the subject of a future study.

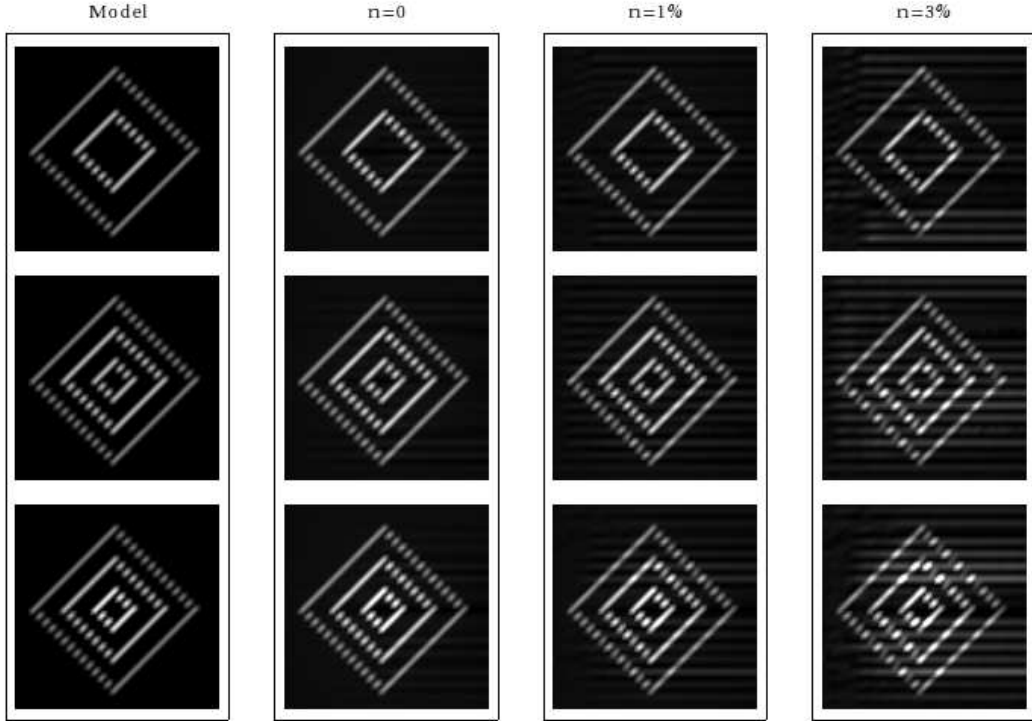


FIG. 15: (Color online) Image reconstruction for the scattering coefficient  $\mu_s$  for an inhomogeneously scattering and absorbing sample and for various noise levels  $n$ . The rows show the slices  $x = 6h$ ,  $13h$  and  $20h$ , where the inhomogeneities are placed. The background scattering and absorption coefficients are set such that  $\bar{\mu}_s L_z = 1.6$  and  $\bar{\mu}_a = \bar{\mu}_s$ , the contrast in  $\mu_s$  varies from 2 to 3, and the contrast in  $\mu_a$  varies from 2 to 5.

### Acknowledgment

This work was supported by the National Science Foundation under Grant No. 0615857

- 
- [1] M.C.W. van Rossum and Th.M. Nieuwenhuizen, *Rev. Mod. Phys.* **71**, 313 (1999).
  - [2] T. Wilson and C.J.R. Sheppard, *Theory and Practice of Scanning Optical Microscopy* (Academic Press, 1984).
  - [3] J.A. Izatt, M.R. Hee, G.M. Owen, E.A. Swanson, and J.G. Fujimoto, *Opt. Lett.* **19**, 590 (1994).
  - [4] J. Sharpe, U. Ahlgren, P. Perry, B. Hill, A. Ross, J. Hecksher-Sorensen, R. Baldock and D.

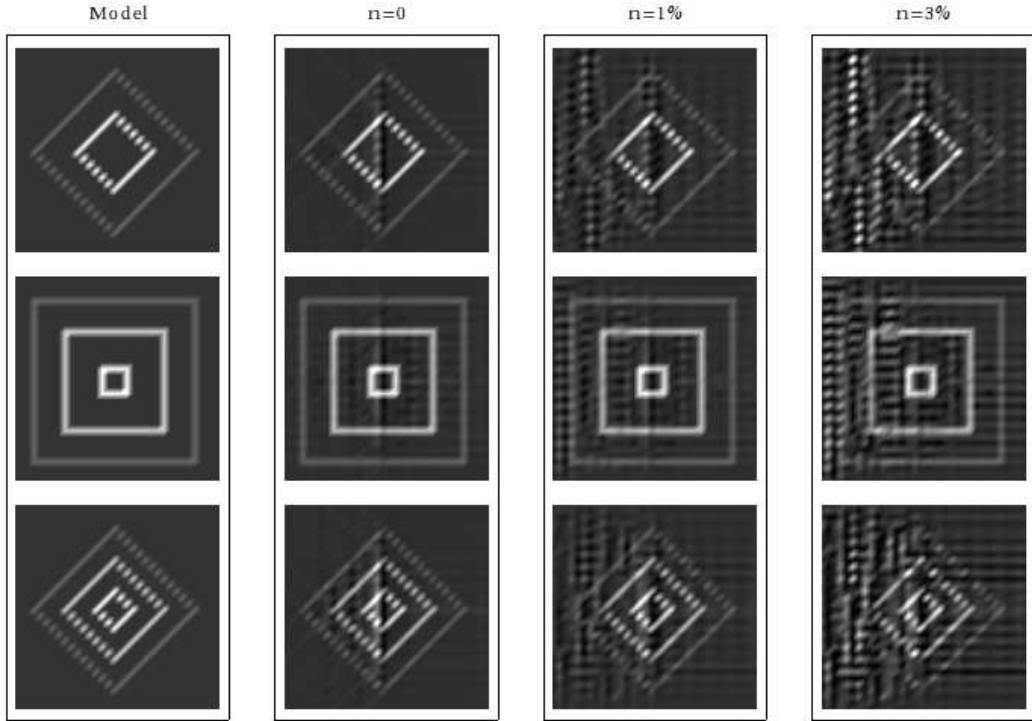


FIG. 16: (Color online) Image reconstruction for the absorption coefficient  $\mu_a$  for an inhomogeneously scattering and absorbing sample and for various noise levels  $n$ . The rows show the slices  $x = 6h$ ,  $13h$  and  $20h$ , where the inhomogeneities are placed. The background scattering and absorption coefficients are set such that  $\bar{\mu}_s L_z = 1.6$  and  $\bar{\mu}_a = \bar{\mu}_s$ , the contrast in  $\mu_s$  varies from 2 to 3, and the contrast in  $\mu_a$  varies from 2 to 5.

Davidson, *Science* **296**, 541 (2002).

- [5] T.S. Ralston, D.L. Marks, P.S. Carney and S.A. Boppart, *J. Opt. Soc. Am. A* **23**, 1027(2006).
- [6] T.S. Ralston, D.L. Marks, P.S. Carney and S.A. Boppart, *Nature Physics* **3**, 129 (2007).
- [7] S. Arridge, *Inv. Prob.* **15**, R41 (1999).
- [8] L. Florescu, J. C. Schotland, V. A. Markel
- [9] F. Natterer and F. Wubbeling, *Mathematical methods in image reconstruction*. Philadelphia: SIAM, 2001.
- [10] A. J. Welch and M. J. C. van Gemert, *Optical-thermal response of laser-irradiated tissue* (Plenum Press, 1995)
- [11] A. Ishimaru, *Wave Propagation and Scattering in random Media* (IEEE, 1997).

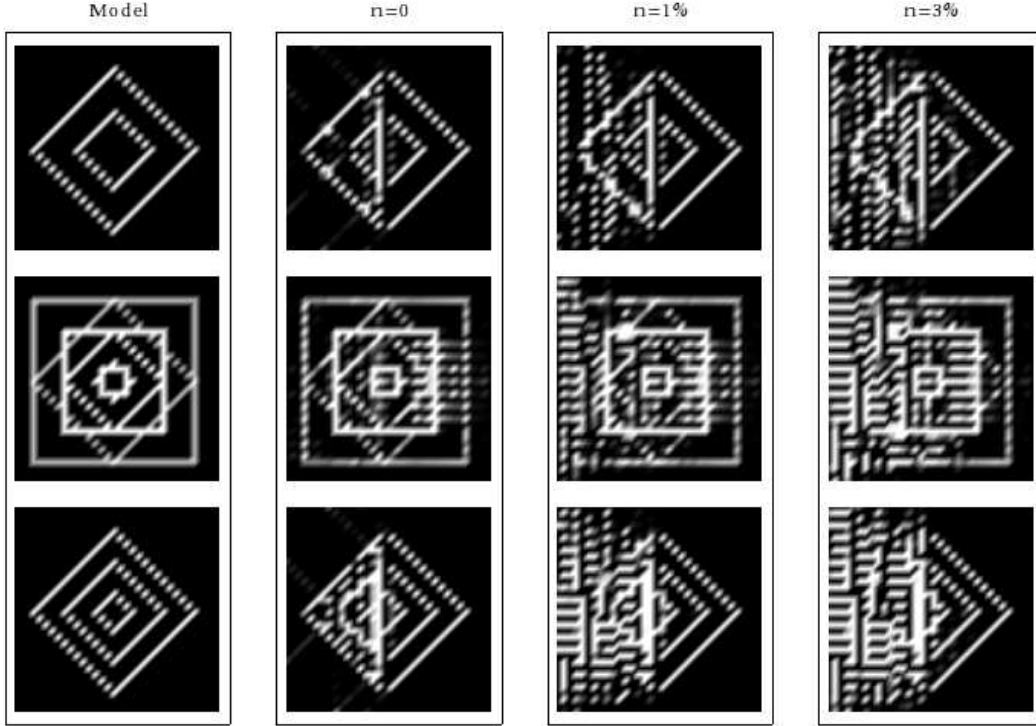


FIG. 17: (Color online) Image reconstruction for the total attenuation coefficient  $\mu_t$  for an inhomogeneously scattering and absorbing sample and for various noise levels  $n$ . The rows show the slices  $x = 6h$ ,  $13h$  and  $20h$ , where the inhomogeneities are placed. The background scattering and absorption coefficients are set such that  $\bar{\mu}_s L_z = 3.2$  and  $\bar{\mu}_a = \bar{\mu}_s$ , the contrast in  $\mu_s$  varies from 2 to 3, the contrast in  $\mu_a$  varies from 2 to 5, and the contrast in  $\mu_t$  varies from 2 to 4.

- [12] J. C. Schotland and V. A. Markel, *J. Opt. Soc. Am. A*, vol. 18, no. 11, pp. 2767–2777, 2001.
- [13] V. A. Markel and J. C. Schotland, *Phys. Rev. E*, vol. 70, no. 5, p. 056616(19), 2004.
- [14] R. C. Erdmann and C. E. Siewert, *J. Math. Phys.*, vol. 9, no. 1, pp. 81–89, 1968.
- [15] E. W. Larsen, *J. Math. Phys.*, vol. 15, no. 3, pp. 299–305, 1974.
- [16] C. Vinegoni, C. Pitsouli, D. Razansky, N. Perrimon, V. Ntziachristos, *Nature Methods* **5**, 45 (2008).

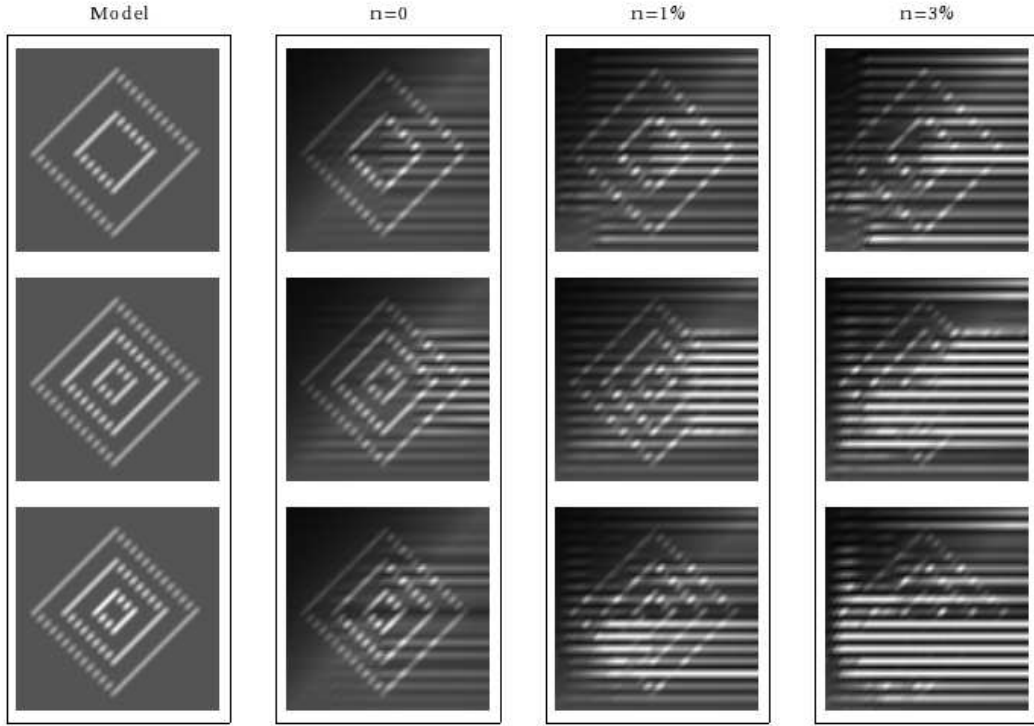


FIG. 18: (Color online) Image reconstruction for the scattering coefficient  $\mu_s$  for an inhomogeneously scattering and absorbing sample and for various noise levels  $n$ . The rows show the slices  $x = 6h$ ,  $13h$  and  $20h$ , where the inhomogeneities are placed. The background scattering and absorption coefficients are set such that  $\bar{\mu}_s L_z = 3.2$  and  $\bar{\mu}_a = \bar{\mu}_s$ , the contrast in  $\mu_s$  varies from 2 to 3, and the contrast in  $\mu_a$  varies from 2 to 5.

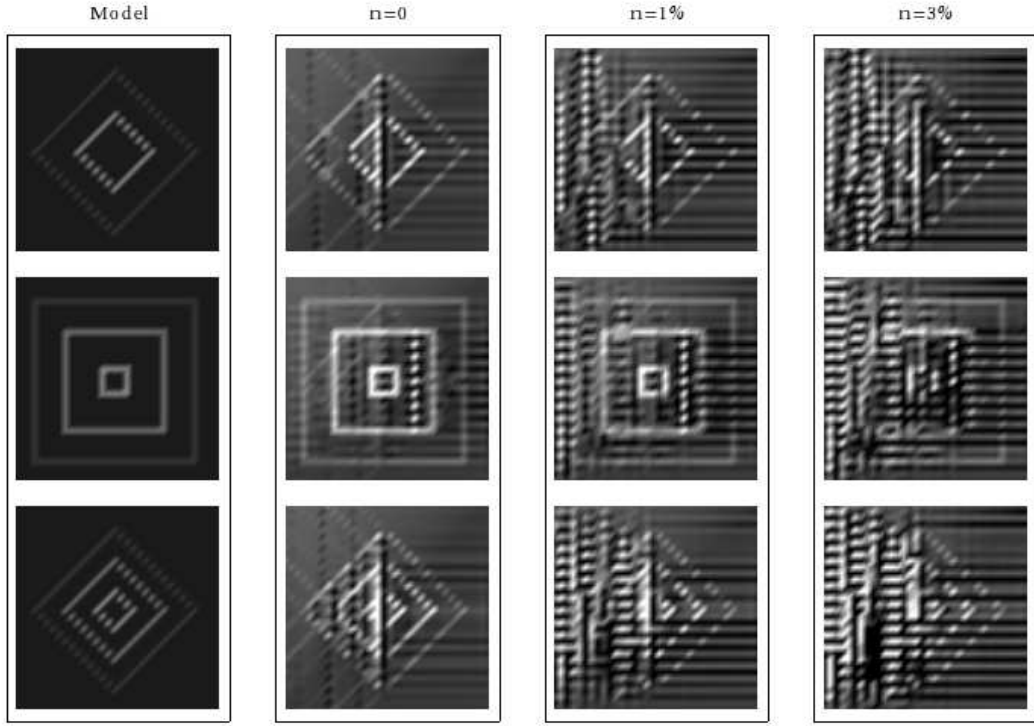


FIG. 19: (Color online) Image reconstruction for the absorption coefficient  $\mu_a$  for an inhomogeneously scattering and absorbing sample and for various noise levels  $n$ . The rows show the slices  $x = 6h$ ,  $13h$  and  $20h$ , where the inhomogeneities are placed. The background scattering and absorption coefficients are set such that  $\bar{\mu}_s L_z = 3.2$  and  $\bar{\mu}_a = \bar{\mu}_s$ , the contrast in  $\mu_s$  varies from 2 to 3, and the contrast in  $\mu_a$  varies from 2 to 5.